Absence of structural correlations of magnetic defects in the heavy-fermion compound LiV_2O_4

S. Das, A. Kreyssig, S. Nandi, A. I. Goldman, and D. C. Johnston
Ames Laboratory and Department of Physics and Astronomy, Iowa State University, Ames, Iowa 50011, USA
(Received 18 November 2008; revised manuscript received 22 July 2009; published 1 September 2009)

Magnetic defects arising from structural imperfections have pronounced effects on the magnetic properties of the face-centered cubic normal-spinel structure compound LiV_2O_4. High-energy x-ray diffraction studies were performed on LiV_2O_4 single crystals to search for superstructure peaks or other evidence of spatial correlations in the arrangement of the crystal defects present in the lattice. Entire reciprocal lattice planes were mapped out with the help of synchrotron radiation. No noticeable differences in the x-ray diffraction data between a crystal with high magnetic defect concentration and a crystal with low magnetic defect concentration were found. This indicates the absence of any long-range periodicity or short-range correlations in the arrangements of the crystal/magnetic defects.

DOI: 10.1103/PhysRevB.80.104401 PACS number(s): 75.20.Hr, 61.72.Dd, 61.72.J−

I. INTRODUCTION

LiV_2O_4 is a material of great interest as it shows heavy fermion behavior at low temperatures ($T \lesssim 10$ K) in spite of being a *d*-electron metal.[1] This is of particular interest because most of the well known heavy fermion compounds have crystallographically ordered arrays of *f*-electron atoms. LiV_2O_4 has a face-centered-cubic crystal structure (space group $Fd\bar{3}m$) with room-temperature lattice parameters $a=b=c=8.2393$ Å.[1] Each V atom is coordinated with six O atoms to form a slightly distorted octahedron.[2] The V atoms themselves form corner sharing tetrahedra, often called the "pyrochlore lattice," which is strongly geometrically frustrated for antiferromagnetic ordering. The vanadium atoms with nominal oxidation state of +3.5 occupy equivalent sites in the structure, making LiV_2O_4 metallic. The heavy fermion nature of LiV_2O_4 was discovered to occur below ~10 K from measurements of a large *T*-independent magnetic susceptibility $\chi \sim 0.01$ cm^3/mol and a large Sommerfeld heat capacity coefficient $\gamma \sim 420$ mJ/mol K^2.[1]

Magnetic defects in the structure have a pronounced effect on the magnetic properties of LiV_2O_4. For both polycrystalline samples and single crystals with extremely low magnetic defect concentration ($n_{defect} \leq 0.01$ mol %), the low-*T* χ is *T* independent.[1,3–5] The heavy fermion behavior of LiV_2O_4 referred to above was inferred from measurements on such samples with extremely low n_{defect}. However, in both powder and single crystal samples of LiV_2O_4 with high n_{defect} (up to a maximum of 0.8 mol %), the magnetic susceptibility shows a Curie-like upturn at low *T*.[1–4] Crystal defects are the only possible source of these magnetic defects since magnetic impurity phases as the source of the low-*T* Curie-like upturn was ruled out.[3,4] Low-*T* magnetization measurements on polycrystalline and single-crystal LiV_2O_4 samples containing magnetic defects revealed large values of the average spins of these defects.[2–4] The spin values S_{defect} range from ~2 to 4.

The presence of magnetic defects has a dramatic influence on ^{7}Li NMR measurements of LiV_2O_4. NMR measurements on polycrystalline samples of LiV_2O_4 with extremely low n_{defect} show a linear variation in the ^{7}Li nuclear spin-lattice relaxation rate $(1/T_1)$ versus *T* at low *T*.[6] This is typical for Fermi liquids. However, for polycrystalline samples of LiV_2O_4 with higher amounts of magnetic defects, the ^{7}Li $1/T_1$ shows a peak at ~1 K, and the relaxation recovery becomes strongly nonexponential.[6,7] This observation raises the question whether the ground state of a LiV_2O_4 sample with high n_{defect} is still a Fermi liquid or is a non-Fermi liquid. If the ground state changes to a non-Fermi liquid, then there might be a critical n_{defect} for the transition. The ^{7}Li NMR measurements indicated that the heavy Fermi liquid survives in the presence of a large concentration of magnetic defects.[7] Johnston *et al.*[6] suggested a model in which a crystal defect locally lifts the geometric frustration and thus allows magnetic order over a finite region around that defect, called a magnetic droplet. This model is qualitatively consistent with the large average values of $S_{defect} \sim 2-4$ obtained from the low-*T* magnetization measurements.

The only potential local magnetic moments in the system are V^{+3} ($S=1$) and V^{+4} ($S=1/2$) and from the observed values $S_{defect} \sim 2-4$ of the spins of the magnetic defects, it is clear that a single V ion cannot give rise to a magnetic defect. The magnetic defects could be a group of V ions forming a cluster or having correlations among them. Given the pronounced effects of the magnetic defects on the properties of LiV_2O_4, it is important to examine if there are any correlations in the spatial distribution of the crystal defects which produce the magnetic defects or if they are randomly distributed. One way to look for short- and medium-range spatial correlations in the defect structure is to map out complete reciprocal lattice planes and search for features in addition to the normal Bragg reflections. Long-range periodic ordering of the crystal defects would produce additional peaks in the x-ray diffraction patterns while short-range ordering can cause streaking of the Bragg peaks or diffuse broad signals. Here we report on high-energy x-ray studies of single crystals of LiV_2O_4 with different magnetic defect concentrations.

II. EXPERIMENTAL DETAILS

High quality single crystals of LiV_2O_4 used in the experiment were grown in a vertical tube furnace using Li_3VO_4 as flux.[2] Three crystals, denoted as crystal 2, crystal 9, and crys-

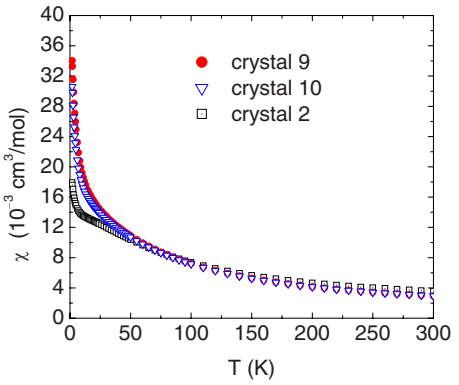

FIG. 1. (Color online) Magnetic susceptibilities χ versus temperature T of LiV_2O_4 crystals containing different concentrations of magnetic defects (see Table I). The susceptibilities are measured in 1 T magnetic field.

tal 10, with respective masses of 0.354, 6.548, and 2.1 mg, were examined. The magnetic measurements on the crystals were done using a Quantum Design superconducting quantum interference device magnetometer in the temperature range of 1.8–350 K and magnetic field range of 0–5.5 T. The studied single crystals were selected based on typical magnetic behavior for low and high defect concentration. Crystals used in the measurements were of different sizes and shapes since as-grown crystals were used. Cutting or polishing the crystals would have given them a common size and shape and improve a quantitative analysis of the scattering data, but at the same time, this procedure had the potential to introduce additional crystal deformations due to strain and/or other mechanical effects. These could obscure the features due to the magnetic defects. We, therefore, decided on using as-grown single crystals. The high-energy x-ray diffraction measurements at room temperature were performed at the 6-ID-D station in the MU-CAT sector of the Advanced Photon Source, Argonne National Laboratory. The incident x-ray energy was set to 100 keV to ensure full penetration of the sample. The corresponding x-ray wavelength λ was 0.124 Å. The beam size was 0.3×0.3 mm^2. To record the full two-dimensional patterns, a MAR345 image-plate was positioned 705 mm behind the sample. During the experiments, the crystals were set between two pieces of thin kapton film and mounted on the sample holder.

III. MAGNETIC SUSCEPTIBILITY AND MAGNETIZATION

Figure 1 shows the magnetic susceptibility χ versus temperature T of the crystals 2, 9, and 10 measured in a 1 T magnetic field. The magnetic defect concentrations of the crystals were calculated by fitting the observed molar magnetization M isotherms at low temperatures [$T\leq5$ K, shown in Figs. 2(a)–2(c)] by the equation[3,4]

$$M = \chi H + n_{\text{defect}} N_A g_{\text{defect}} \mu_B S_{\text{defect}} B_S(x), \quad (1)$$

where n_{defect} is the concentration of the magnetic defects, N_A is Avogadro's number, g_{defect} is the g factor, which was fixed to 2 for the spins of the magnetic defects (the detailed reasoning behind this is given in Ref. 3), μ_B is the Bohr magneton, S_{defect} is the average spin of the defects, $B_S(x)$ is the Brillouin function, χ is the intrinsic susceptibility of the pure LiV_2O_4 spinel phase in the absence of magnetic defects, and H is the applied magnetic field. The argument of the Brillouin function $B_S(x)$ is $x=g_{\text{defect}}\mu_B S_{\text{defect}} H/[k_B(T-\theta_{\text{defect}})]$ where θ_{defect} is the Weiss temperature associated with the magnetic defects and k_B is Boltzmann's constant. The parameters fitted are χ, n_{defect}, S_{defect}, and θ_{defect}.

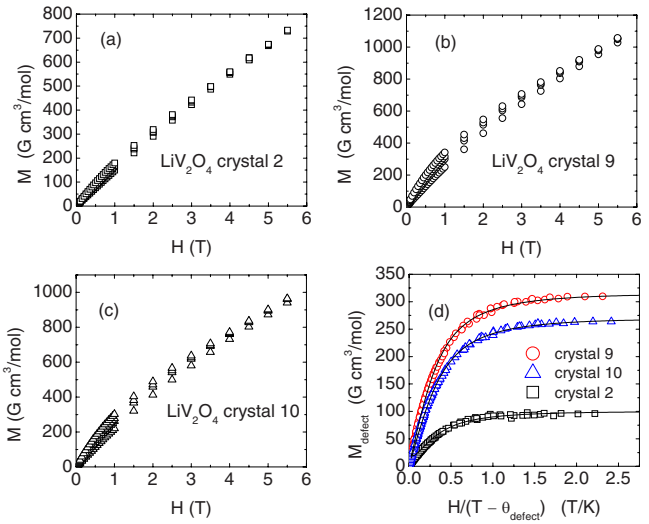

FIG. 2. (Color online) Molar magnetization M versus applied magnetic field H isotherms at low temperatures ($T\leq5$ K) for crystals (a) 2, (b) 9, and (c) 10, respectively. The four data sets shown in each of Figs. 2(a)–2(c) are the $M(H)$ isotherms at four different temperatures 5, 3, 2.5, and 1.8 K. Figure 2(d) shows the magnetic defect contribution to the magnetization for each crystal $M_{\text{defect}}=M-\chi H$ plotted versus $H/(T-\theta_{\text{defect}})$. The solid lines are plots of the second term in Eq. (1) for each crystal with the parameters listed in Table I.

The best-fit parameters obtained from the fits of the $M(H)$ isotherm data in Figs. 2(a)–2(c) by Eq. (1) are tabulated in Table I for each crystal. Figure 2(d) shows the defect contributions to the magnetization $M_{\text{defect}}=M-\chi H$ for each crystal plotted versus $H/(T-\theta_{\text{defect}})$. All the data points in Figs. 2(a)–2(c) collapse onto a universal curve for each crystal, thus verifying the validity of the model and the fits. The solid lines in Fig. 2(d) are the plots of the second term in Eq. (1) for the three crystals with the parameters listed in Table I,

TABLE I. Magnetic parameters obtained from fits of Eq. (1) to the magnetization versus field measurements below 5 K in Fig. 1 of the three LiV_2O_4 crystals. χ, n_{defect}, S_{defect}, and θ_{defect} are magnetic susceptibility, magnetic defect concentration, spin of the magnetic defects, and Weiss temperature of the interactions among the magnetic defects, respectively. A number in parentheses indicates the error in the last digit of a quantity.

Sample no.	χ (cm^3/mol)	n_{defect} (mol %)	S_{defect}	θ_{defect} (K)	$n_{\text{defect}}S_{\text{defect}}$ (mol %)
crystal 2	0.01158(6)	0.24(1)	3.6(2)	−0.7(1)	0.86(1)
crystal 9	0.0135(1)	0.71(3)	3.9(1)	−0.6(1)	2.78(7)
crystal 10	0.0127(1)	0.67(2)	3.6(1)	−0.5(1)	2.38(6)

respectively. Note that χ in Table I is constant to within $\pm 8\%$ as n_{defect} increases by nearly a factor of three. This indicates that the heavy Fermi liquid survives in the presence of the magnetic defects, consistent with the ^{7}Li NMR analysis in Ref. 7.

IV. HIGH-ENERGY X-RAY DIFFRACTION MEASUREMENT

In order to search for long-range or short-range order in the arrangement of the crystal defects giving rise to the magnetic defects within the crystal structure, we carried out high-energy synchrotron x-ray diffraction measurements over a wide range of reciprocal space. The rocking technique used to record the diffraction intensities from planes in reciprocal space has been described in detail in Ref. 8. Briefly, the patterns were obtained by recording the Bragg reflections of all points of a reciprocal lattice plane intersecting the Ewald sphere. The orientation of the reciprocal lattice relative to the Ewald sphere is given by the orientation of the crystal with respect to the incident x-ray beam. Tilting the crystal through small angles allows complete reciprocal lattice planes of the crystal to intersect the Ewald sphere. In the experiment, diffraction patterns were obtained as in Fig. 3 below by tilting the crystal through two independent angles μ and η perpendicular to the incident x-ray beam by $\pm 3.2°$. Patterns were recorded by continuously scanning through μ as η was increased in small steps. By averaging the recorded patterns obtained at different values of μ and η, a considerable range of the designated reciprocal lattice planes was mapped out. This averaging over large parts of a Brillouin zone also enhances very weak broad scattering features making them detectable.

Depending on the kind of modification/deviation of the crystal structure arising from the crystal defects, we expect to see different modifications/deviations in the diffraction patterns of the reciprocal planes. A crystallographic superstructure, either commensurate or incommensurate, will produce weak additional Bragg reflections. Lower-dimensional or short-range order will produce broad features or diffuse scattering. For example, a two-dimensional order yields a rodlike scattering feature. If the incoming beam is parallel to the axis of the rod, we will see a spot in the diffraction pattern of that plane. The same feature, however, will yield a streak of intensity in the diffraction patterns of reciprocal planes perpendicular to the rod.

In our experiment, reflections from reciprocal lattice planes perpendicular to the three high symmetry directions, namely, [001], $[\bar{1}01]$, and $[\bar{1}\bar{1}1]$ of the cubic structure, were recorded. Figures 3(a)–3(c) show the room-temperature diffraction patterns from planes in the reciprocal space of crystal 2 ($n_{\text{defect}}=0.24$ mol %) perpendicular to the [001], $[\bar{1}01]$, and $[\bar{1}\bar{1}1]$ directions, respectively. The lattice planes perpendicular to the $[\bar{1}\bar{1}1]$ direction are very closely spaced. Thus in this direction, when we tilt the crystal, higher order reciprocal planes will also intersect the Ewald sphere and be observed.[8] This out-of-plane scattering was minimized by limiting the range of the tilts to $\pm 2.8°$. Nevertheless, the

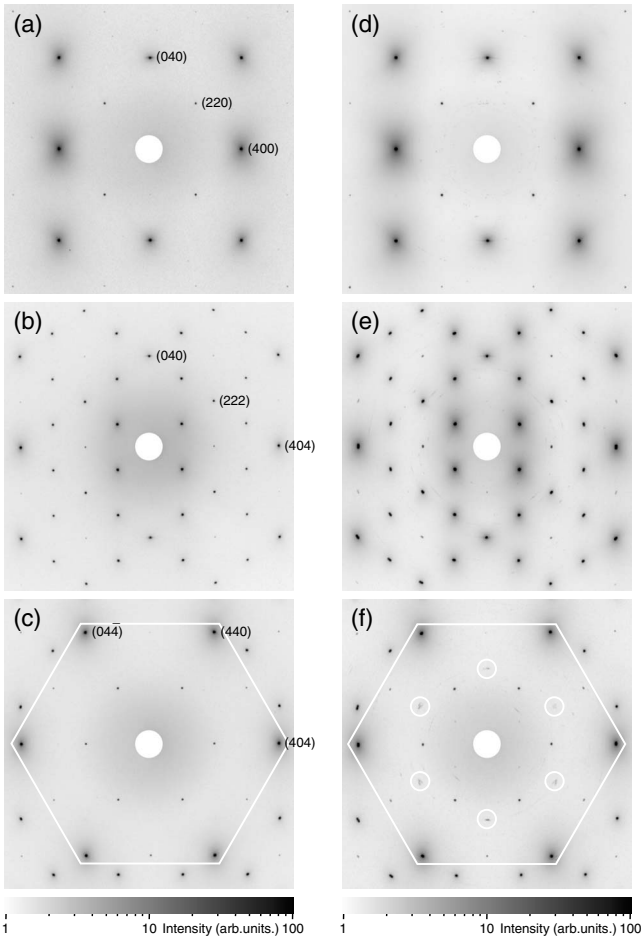

FIG. 3. High-energy x-ray diffraction patterns of LiV_2O_4 single crystals 2 and 9. Figures 3(a)–3(c) show the patterns for reciprocal planes of crystal 2 perpendicular to the [001], $[\bar{1}01]$, and $[\bar{1}\bar{1}1]$ directions, respectively. Figures 3(d)–3(f) show the patterns for reciprocal planes of crystal 9 perpendicular to the [001], $[\bar{1}01]$, and $[\bar{1}\bar{1}1]$ directions, respectively. In (f), the extended features indicated by white circles are reflections that are not allowed by the symmetry. The reflection spots enclosed by the white lines in (c) and (f) are from the reciprocal (hkl) layer through the origin which is perpendicular to the $[\bar{1}\bar{1}1]$ direction with $(hkl)\cdot[\bar{1}\bar{1}1]=0$. The outer spots are from the next layers with $(hkl)\cdot[\bar{1}\bar{1}1]=\pm 1$. The patterns shown have the same aspect ratio as that of the patterns recorded in the detector.

reflections enclosed by the white lines in (c) and (f) are from the reciprocal layer through the origin, which is perpendicular to the $(\bar{1}\bar{1}1)$ direction $[(hkl)$ reflections with $(hkl)\cdot[\bar{1}\bar{1}1]=0]$. The outer spots are from the next layers $[(hkl)\cdot[\bar{1}\bar{1}1]=\pm 1]$.

In Figs. 3(a)–3(c), all the spots observed are allowed by the space group of the crystal. The intensity at the center of the Bragg reflections are 3–6 orders of magnitude higher than the intensity shown in black at the maximum in the scale for the contour map. We used iron slabs, up to 3 cm in thickness, to increase the dynamic range from 10^4 (intrinsic for the detector) to 10^7 by attenuating the incident x-ray beam. The gray tone in Fig. 3 represents the intensity on a

logarithmic scale. In each pattern, the scale has been chosen in such a manner that as much as possible, the details in low signals can be visualized. No extra spots or Bragg reflections were observed in the patterns. We conclude that there are no other single crystals or grains oriented in other directions or satellite reflections related to a superstructure of the given normal spinel structure. The shape of the spots is also as expected for the given resolution conditions.

Figures 3(d)–3(f) show the room-temperature x-ray diffraction patterns from reciprocal planes of crystal 9 with high magnetic defect concentration (n_{defect}=0.62 mol %) perpendicular to the [001], [$\bar{1}$01], and [$\bar{1}$11] directions, respectively. For the planes perpendicular to the [001] and [$\bar{1}$01] directions, there are no differences between the patterns obtained for crystal 2 and crystal 9. From the positions of the Bragg reflections, the lattice parameters of these two crystals are the same to within our precision of one part in one thousand. For the plane perpendicular to the [$\bar{1}$11] direction, a few spots were observed, marked by solid circles in Fig. 3(f), which are not allowed by the symmetry of the space group and are missing in Fig. 3(c). These extra features are linearly extended compared to the circular spots and have an intensity 10^{-5} times that of the Bragg reflections. The position of these extra spots is close to the expected position of reflections from higher layers [e.g., (311) and symmetry equivalent reflections]. By reducing or increasing the range of the rocking angles, the contribution from the higher layers can be modified. The intensity and shape of the additional features did not change when the patterns were recorded with different ranges for the rocking angles. This suggests that the additional features are located on the reciprocal plane close to the origin and eliminates significant contributions from Bragg reflections of higher layers or from the halos around them. We note that twinning or stacking faults of similarly oriented crystals can allow such features to appear. Furthermore, as seen from the spots outside the white polygon, these features are not present in the other Brillouin zones with the same orientation. This excludes the possibility of periodic arrangement of such crystal defects.

The observed halos surrounding the Bragg reflections are partially caused by exposure of the adjacent pixels in the detector material due to light scattering between pixels within the detector for strong signals. The diffuse scattering dominating at lower count rates also contributes to the formation of the halos. Distinguishing between diffuse scattering arising from static disorder and thermal diffuse scattering arising from uncorrelated lattice vibrations would require extensive temperature-dependent studies including detailed two-dimensional profile analysis and is beyond the scope of the present study. The halos around the Bragg reflections are similar for both samples with high and low magnetic defect concentrations, respectively. Unfortunately, the visibility of the halos in the different patterns is handicapped by the different signal to background ratios which vary by up to a factor of twenty between the different patterns. This is due to different sizes and shapes of the samples and the resulting different scattering strengths of the samples and different absorptions of the primary beam and background signals. As a consequence, the halos in Fig. 3(b) are barely visible and barely separable from the background signal. A comparison of the intensity of the halos around strong reflections [e.g., (404) and (131)] with the intensity of the Bragg reflections themselves yields a similar ratio for both samples for patterns measured perpendicular to the [$\bar{1}$01] direction shown in Figs. 3(b) and 3(e). The intensities at several data points in the halo of each Bragg reflection were compared with the maximum value in the center of the Bragg reflection itself. As long as the count rate in the halo was significantly above the background from incoherent and air scattering and the reflections were of comparable strength, the variation in the ratio was minimal. The ratio deviates slightly (by up to a factor of 1.6) for strong reflections, likely due to extinction effects. A comparison of the intensity of the halos and that of the corresponding Bragg reflections shows no obvious deviation from the expected scaling between the intensities. The similarity in the strength of the halos relative to the Bragg reflections for both types of samples, with low and high magnetic defect concentrations, suggests that the diffuse scattering is likely dominated by thermal diffuse scattering and cannot explain the observed difference in their magnetic properties.

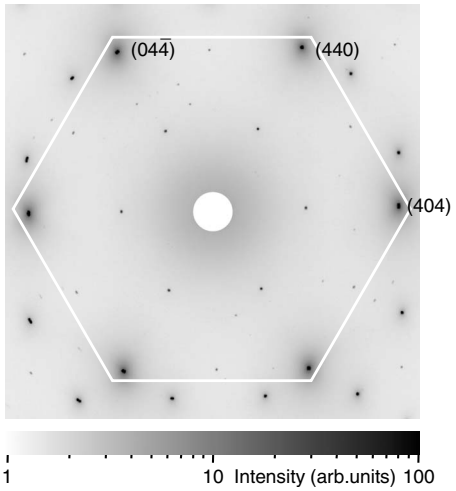

FIG. 4. High-energy x-ray diffraction pattern of the reciprocal lattice plane perpendicular to the [$\bar{1}$11] direction of LiV_2O_4 crystal 10.

To test if the appearance of the extended extra features for crystal 9 [shown in Fig. 3(f)] is an artifact of the particular crystal or is intrinsic, we performed the same experiment on crystal 10 which was grown under similar conditions and has a similar magnetic defect concentration as that of crystal 9. The x-ray diffraction pattern for the reciprocal lattice plane perpendicular to the [$\bar{1}$11] direction of crystal 10 is shown in Fig. 4. We note that the additional spots present in Fig. 3(f) are missing here. There are a few very weak spots other than those allowed for the plane perpendicular to the [$\bar{1}$11] direction. These are caused by other misaligned crystals of the same material or impurities and illustrate the very high sensitivity of the technique to the smallest deviations/differences in the pattern from that expected for a perfect crystal. If we focus our beam onto different spots on the same crystal surface, the extra peaks vary in intensity or disappear.

V. SUMMARY

No noticeable difference in the high-energy x-ray diffraction patterns of the reciprocal lattice planes of a crystal with high magnetic defect concentration and a crystal with low magnetic defect concentration has been found. This indicates the absence of any long-range periodicity or order in the arrangement of the crystal defects giving rise to the magnetic defects. We also did not observe any difference in the diffuse scattering in reciprocal space for both samples and thus exclude any long-range low-dimensional order or short-range order of the crystal defects related to the different magnetic defect concentrations. Thus we conclude that the crystal defects in LiV_2O_4 which produce the magnetic defects are randomly distributed within the spinel structure.

ACKNOWLEDGMENTS

We thank D. Robinson for assistance with the x-ray diffraction measurements at the Advanced Photon Source. Work at the Ames Laboratory was supported by the Department of Energy–Basic Energy Sciences under Contract No. DE-AC02-07CH11358. Use of the Advanced Photon Source (APS) was supported by the U.S. Department of Energy, Office of Science, under Contract No. DE-AC02-06CH11357. The Midwest Universities Collaborative Access Team (MUCAT) sector at the APS is supported by the U.S. Department of Energy, Office of Science, through the Ames Laboratory under Contract No. DE-AC02-07CH11358.

[1] S. Kondo, D. C. Johnston, C. A. Swenson, F. Borsa, A. V. Mahajan, L. L. Miller, T. Gu, A. I. Goldman, M. B. Maple, D. A. Gajewski, E. J. Freeman, N. R. Dilley, R. P. Dickey, J. Merrin, K. Kojima, G. M. Luke, Y. J. Uemura, O. Chmaissem, and J. D. Jorgensen, Phys. Rev. Lett. **78**, 3729 (1997).

[2] S. Das, X. Zong, A. Niazi, A. Ellern, J. Q. Yan, and D. C. Johnston, Phys. Rev. B **76**, 054418 (2007).

[3] S. Kondo, D. C. Johnston, and L. L. Miller, Phys. Rev. B **59**, 2609 (1999).

[4] S. Das, X. Ma, X. Zong, A. Niazi, and D. C. Johnston, Phys. Rev. B **74**, 184417 (2006).

[5] Y. Matsushita, H. Ueda, and Y. Ueda, Nature Mater. **4**, 845 (2005).

[6] D. C. Johnston, S. H. Baek, X. Zong, F. Borsa, J. Schmalian, and S. Kondo, Phys. Rev. Lett. **95**, 176408 (2005).

[7] X. Zong, S. Das, F. Borsa, M. D. Vannette, R. Prozorov, J. Schmalian, and D. C. Johnston, Phys. Rev. B **77**, 144419 (2008).

[8] A. Kreyssig, S. Chang, Y. Janssen, J. W. Kim, S. Nandi, J. Q. Yan, L. Tan, R. J. McQueeney, P. C. Canfield, and A. I. Goldman, Phys. Rev. B **76**, 054421 (2007).